HAL
open science

Mononuclear Ni(II) Complexes with a S3O Coordination Sphere Based on a Tripodal Cysteine-Rich Ligand: pH Tuning of the Superoxide Dismutase Activity

Jérémy Domergue, Jacques Pécaut, Olivier Proux, Colette Lebrun, Christelle Gateau, Alan Le Goff, Pascale Maldivi, Carole Duboc, Pascale Delangle

▶ To cite this version:

Jérémy Domergue, Jacques Pécaut, Olivier Proux, Colette Lebrun, Christelle Gateau, et al.. Mononuclear Ni(II) Complexes with a S3O Coordination Sphere Based on a Tripodal Cysteine-Rich Ligand: pH Tuning of the Superoxide Dismutase Activity. Inorganic Chemistry, 2019, 58 (19), pp.12775-12785. 10.1021/acs.inorgchem.9b01686 . hal-02389143

HAL Id: hal-02389143

https://hal.science/hal-02389143v1

Submitted on 19 Nov 2020

HAL is a multi-disciplinary open access archive for the deposit and dissemination of scientific research documents, whether they are published or not. The documents may come from teaching and research institutions in France or abroad, or from public or private research centers.

L'archive ouverte pluridisciplinaire **HAL**, est destinée au dépôt et à la diffusion de documents scientifiques de niveau recherche, publiés ou non, émanant des établissements d'enseignement et de recherche français ou étrangers, des laboratoires publics ou privés.

Mononuclear Ni(II) complexes with a S3O coordination sphere based on a tripodal cysteine-rich ligand: pH tuning of the SOD activity

Jérémy Domergue,[a,b] Jacques Pécaut,[b] Olivier Proux,[c] Colette Lebrun,[b] Christelle Gateau,[b] Alan Le Goff,[a] Pascale Maldivi,[b] Carole Duboc,[a,*] Pascale Delangle[b,*]

[a] *Univ. Grenoble Alpes, CNRS, DCM, 38000 Grenoble, France*
[b] *Univ. Grenoble Alpes, CEA, CNRS, SyMMES, 38000 Grenoble, France*
[c] *Univ. Grenoble Alpes, CNRS, OSUG, 38000 Grenoble, France*
Corresponding authors, carole.duboc@univ-grenoble-alpes.fr, pascale.delangle@cea.fr

Abstract.

The superoxyde dismutase (SOD) activity of mononuclear Ni^{II} complexes, whose structures are inspired by the NiSOD, has been investigated. They have been designed with a sulfur-rich pseudo-peptide ligand, derived from nitrilotriacetic acid (NTA), where the three acid functions are grafted with cysteines (**L^{3S}**). Two mononuclear complexes, which exist in pH-dependent proportions, have been fully characterized by a combination of spectroscopic techniques including ^{1}H NMR, UV-vis, CD, and XAS, together with theoretical calculations. They display similar square-planar S3O coordination, with the three thiolates of the three cysteine moieties from **L^{3S}** coordinated to the Ni^{II} ion, together with either a water molecule at physiological pH, as [Ni**L^{3S}**(OH_2)]$^-$, or a hydroxo ion in more basic conditions, as [Ni**L^{3S}**(OH)]$^{2-}$. The ^{1}H NMR study has revealed that contrary to the hydroxo ligand, the bound water molecule is labile. The CV of both complexes displays an irreversible one-electron oxidation process assigned to the Ni^{II}/Ni^{III} redox system with E_{pa} = 0.48 and 0.31 V vs SCE for Ni**L^{3S}**(OH_2) and Ni**L^{3S}**(OH), respectively. The SOD activity of both complexes has been tested. Based on the xanthine oxidase assay, an IC_{50} of about 1 μM has been measured at pH 7.4, where Ni**L^{3S}**(OH_2) is mainly present (93% of the Ni^{II} species), while the IC_{50} is larger than 100 μM at pH 9.6, where Ni**L^{3S}**(OH) is the major species (92% of the Ni^{II} species). Interestingly, only Ni**L^{3S}**(OH_2) displays SOD activity, suggesting that the presence of a labile ligand is required. The SOD activity has been also evaluated under catalytic conditions at pH 7.75, where the ratio between Ni**L^{3S}**(OH_2) / Ni**L^{3S}**(OH) is about (86:14), and a rate constant, k_{cat} = 1.8 10^5 $M^{-1}s^{-1}$ has been measured. Ni**L^{3S}**(OH_2) is thus the first low-molecular weight, synthetic, bio-inspired Ni complex that displays catalytic SOD activity in water at physiological pH, although it does not contain any N-donor ligand in its first coordination sphere, as in the NiSOD. Overall, the data evidences that a key structural feature is the presence of a labile ligand in the coordination sphere of the Ni^{II} ion, consistent with an inner sphere mechanism for at least one of the redox reactions.

Introduction

Superoxide Dismutase (SOD) is a key enzyme in all aerobic organisms as it degrades the radical anion superoxide ($O_2^{\bullet-}$), one of the toxic reactive oxygen species (ROS), constantly produced as a by-product during aerobic respiration. In the specific case of $O_2^{\bullet-}$, the SODs protect the cell against severe damage by catalyzing its disproportionation into H_2O_2 and O_2 using a redox-active metallic (M) cofactor (eq. 1 & 2).[1]

$$M^{red}SOD + O_2^{\bullet-} + 2H^+ \rightarrow H_2O_2 + M^{ox}SOD \qquad \text{eq. 1}$$

$$M^{ox}SOD + O_2^{\bullet-} \rightarrow O_2 + M^{red}SOD \qquad \text{eq. 2}$$

With N/O coordination spheres, the metallic cofactors are Mn, Fe, Cu/Zn or Cu only.[2-9] In 1996, a SOD with a thiolate-based Ni complex was discovered.[10] This Ni-SOD has attracted attention of bioinorganic chemists for several reasons. First, this is one of only four enzymes that contain a mononuclear Ni catalytic center (in addition to acireductone dioxygenase, glyoxylase and methyl-coenzyme M reductase).[11] Second, the coordination sphere of the Ni^{II} ion is intriguing with the presence of two cysteinates, bearing in mind that metal-bound thiolates are well known to react with $O_2^{\bullet-}$ and even O_2 and H_2O_2, leading to oxidative damage.[12-13] Third, the coordination sphere of the Ni site is completed by donor ligands from only the first six amino acids of the N terminal part of the peptide chain, in an original motif involving the terminal amine and an amidate in the Ni^{II} reduced state. The square plane around the Ni^{II} ion becomes a square pyramid in the Ni^{III} state, with the additional coordination of an imidazole of a histidine in the axial position (Scheme 1).[14-16] Apart from the characterization of these two states (oxidized and reduced) that are involved in a ping-pong mechanism, nothing is known about the mechanism of the NiSOD.

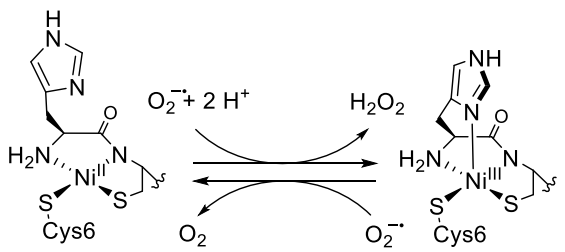

Scheme 1. Active and catalysed reaction centre by the NiSOD

With the aim of better understanding the key-elements of this active site, chemists have designed bio-inspired synthetic complexes to investigate the role of the amidate for the SOD activity, the stability of the thiolates in catalytic conditions, the role of the axial ligand, and finally, the different possible mechanisms to probe inner or outer sphere processes. To address

these questions, two strategies have been followed based on Ni^{II} complexes either designed with peptide-based ligands[17-27] or synthetic ligands.[27-42]

Because only the first residues of the N-terminal part are involved, the reported peptide-based models mainly contain between 7 and 12 residues. They closely reproduce the spectroscopic features of the Ni-SOD and the SOD reactivity, although still with less efficiency.[43] From their investigation, it was evidenced that the presence of a residue that can axially coordinate to the Ni site drastically enhances the activity but is not critical.[44-45] The first series of synthetic bio-inspired complexes have evidenced that mixed amidate/amine coordination sphere allows for fine-tuning the redox properties of the bis-thiolate Ni motif in order to protect, at least partially, sulfur-centered degradation processes.[46-47] The role of the fifth ligand in the axial position to stabilize the Ni^{III} oxidation state has been also reproduced.[35, 41-42] However, the great majority of the low-molecular weight synthetic Ni^{II} complexes, despite their apparent appropriate redox properties for SOD activity, are not active as catalysts even if they can mimic the partial[40-41] or full[48] catalytic cycle under stoichiometric conditions. Their lack of reactivity has often been rationalized either by their sensitivity to the superoxide or derivatives, or by the irreversibility of the Ni^{III}/Ni^{II} redox process.[37] Finally, these two bio-inspired strategies have led to the proposal of different mechanisms for the NiSOD reactivity, with the disproportionation of the superoxide occurring through either inner[24, 40] or outer[48-49] sphere pathways.

To evaluate the importance of the amidate/amine N-donor environment to produce active SOD Ni-based catalysts, we report here the investigation of two mononuclear Ni^{II} SOD catalysts based on a sulfur-rich pseudo-peptide ligand. This so-called pseudo-peptide is derived from nitrilotriacetic acid (NTA), with the three acid functions grafted with cysteines (**L^{3S}** in Scheme 2). Such architectures with amino acids anchored on a tripodal chemical scaffold are highly soluble in water, and hence, their complexes' properties can be studied in conditions relevant to biology. They have been demonstrated to promote the coordination of three sulfur donors from either cysteines, D-penicillamines, or methionines to soft metal ions.[50-55] In particular, the coordination properties of **L^{3S}** for Cu^{I} resemble those of the detoxification proteins, i.e. metallothioneins,[56] and have been exploited to design a very efficient Cu intracellular chelator.[57] **L^{3S}** stabilizes the trigonal planar coordination of Cu^{I} with three thiolates in very stable complexes in water at physiological pH: a mononuclear complex under (sub)stoichiometric conditions of Cu^{I} and a well-defined Cu^{I}-thiolate Cu_6S_9 cluster in excess of Cu^{I}.[51] Interestingly, a similar pseudo-peptide ligand derived from histidine in place of cysteine moieties was demonstrated to coordinate both Cu^{I} and Cu^{II} oxidation states in very different geometries: Cu^{I} was found in a tetrahedral geometry whereas Cu^{II} was demonstrated to be in a distorted square planar geometry.[58] This

highlights the versatility of the coordination environments that can be accessed with such tripodal peptide-like architectures.

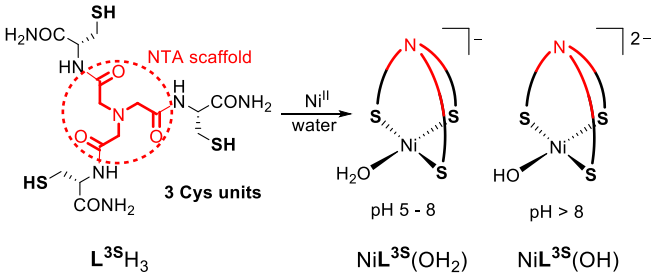

Scheme 2. Structure of the ligand **L^{3S}** and complexes obtained after addition of Ni^{II} under different pH conditions.

Through a detailed spectroscopic investigation, including ^{1}H NMR, UV-vis, CD, and XAS, combined with theoretical calculations, **L^{3S}** is demonstrated here to form two mononuclear Ni^{II} complexes: [Ni**L^{3S}**(OH$_2$)]$^-$ at physiological pH (pH range 5-8) and [Ni**L^{3S}**(OH)]$^{2-}$ in more basic conditions (pH>8) (Scheme 2). For both complexes, a similar S3O coordination sphere with three thiolates originating from the cysteines of the ligand is evidenced, and either a water or a hydroxo molecule, respectively. Despite this sulphur-rich coordination and absence of the mixed amine/amidate environment present in the Ni-SOD, the redox properties of these complexes show that the Ni^{II}/Ni^{III} redox potential is appropriate to disproportionate superoxide. Interestingly, the complex found at physiological pH, Ni**L^{3S}**(OH$_2$), exhibits catalytic SOD activity, whereas the hydroxo species Ni**L^{3S}**(OH) does not. This difference in reactivity is interpreted on the basis of the spectroscopic data.

Results

Evidence for Ni^{II} complex formation with L^{3S} at pH 7.4. The synthesis of the **L^{3S}** ligand has been previously described.[51] Because of the sensitivity of the thiolate-based Cu^{I} complexes and clusters characterized before with **L^{3S}** and derivatives towards O$_2$ oxidation, the investigation of the coordination of Ni^{II} with **L^{3S}** has been carried out under anaerobic conditions. The complexation properties of **L^{3S}** have been studied by UV-visible spectroscopy, since intense ligand-to-metal-charge transfer (LMCT) features from the thiolates to Ni^{II} are expected in the UV region.[59-60] Aliquots of Ni^{II} (NiSO$_4$) have been added to a solution of **L^{3S}** in HEPES buffer (20 mM, pH 7.4, [NaCl]=100 mM), from 0 to 4 equiv. per ligand, and the titration is reported in Figure 1. While the **L^{3S}** solution displays no UV-vis transition above 250 nm, addition of Ni^{II} leads to the appearance of two intense bands at 289 nm (ε = 10 500 M^{-1}cm^{-1}) and 345 nm (ε = 6 300 M^{-1}cm^{-1}), assigned to the expected LMCTs and a broad and less intense band at 462 nm (ε = 1 000 M^{-1}cm^{-1}) that could be tentatively attributed to a d-d transition.[61] The inset of Figure 1 displays the

variations of the molar absorption coefficients (ε) of these main bands with the number of Ni^{II} equiv. added. The regular increase of the ε up to 1 equiv. points to the formation of one complex, which evolves into a second species from 1 to 2 equiv. A plateau is then observed after 2 equiv. These data are consistent with the successive formation of two Ni^{II} complexes depending on the number of equivalents of Ni^{II} per ligand (1 equiv. and 2 equiv., respectively). To confirm this analysis, circular dichroism (CD) experiments have been carried out.

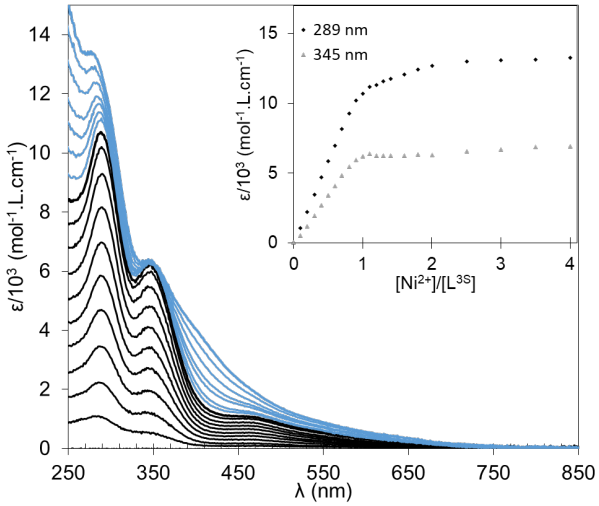

Figure 1. UV titration of $\mathbf{L^{3S}}$ (57 μM) with Ni^{II} at pH 7.4 (20 mM Hepes buffer, 100 mM NaCl). Spectra in black correspond to samples between 0 and 1 equiv. of Ni^{II} per $\mathbf{L^{3S}}$, spectra in blue correspond to samples between 1 and 2 equiv. of Ni^{II}. Inset: evolution of the absorbance at 289 nm and 345 nm.

The CD titration in HEPES buffer (20 mM, pH 7.4, [NaCl]=100 mM) is represented in Figure 2 and confirms the formation of two successive Ni^{II} complexes with notably different CD features. Only one complex is formed in Ni^{II}-limiting conditions as shown by the isodichroic points at 286, 314, and 462 nm. The spectrum is dominated by two main bands at 298 nm (+) and 351 nm (-) that can be attributed to $S^- \rightarrow Ni^{II}$ LMCT,[62] and one at 405 nm (-) assigned to a d-d transition as an indication of a square planar geometry.[63] The spectrum dramatically changes between 1 and 2 Ni^{II} equiv. (main bands in the new spectrum at 248 nm (+), 282 nm (-), 307 nm (-), 378 nm (-), 440 nm (+), 562 nm (+)), with no further evolution with a larger excess of metal ion. Interestingly, isodichroic points (at 333, 357, 404 and 533 nm) are also observed from 1 to 2 equiv. of Ni^{II}, in agreement with an equilibrium between two distinct complexes only. Based on these experiments, it can be proposed that with up to 1 equiv. of Ni^{II}, a mononuclear complex corresponding to a Ni:$\mathbf{L^{3S}}$ 1:1 ratio is exclusively formed. This complex transforms into the higher nuclearity Ni:$\mathbf{L^{3S}}$ 2:1 species in excess of Ni^{II}.

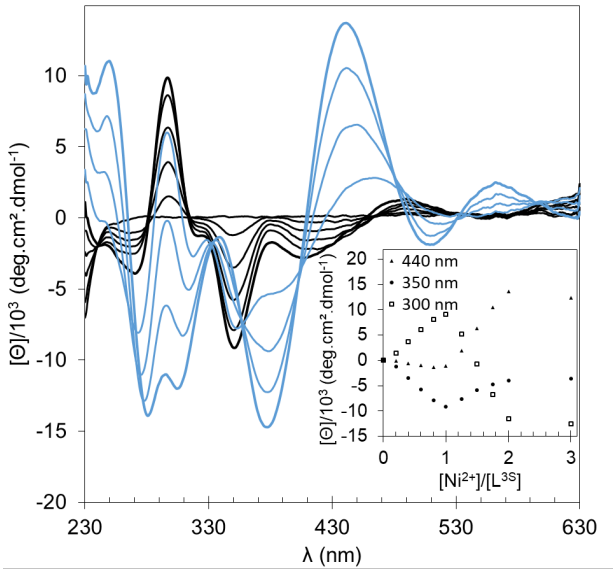

Figure 2. CD titration of $\mathbf{L^{3S}}$ (76 µM) with Ni^{II} at pH 7.4 (20 mM Hepes buffer, 100 mM NaCl). Spectra in black correspond to samples between 0 and 1 equiv. of Ni^{II} per $\mathbf{L^{3S}}$, spectra in blue correspond to samples between 1 and 2 equiv. of Ni^{II}. Inset: evolution of the absorbance at 300 nm, 350 nm and 440 nm.

The electrospray ionization mass spectrometry experiments (ESI-MS) performed in ammonium acetate aqueous solution (20 mM, pH 6.9) are consistent with these spectroscopic observations (Figure S1). Indeed, in Ni^{II} limiting conditions, the main ion detected in the (-)ESI-MS spectrum is $[Ni\mathbf{L^{3S}}]^-$ (m/z = 552.0), with small signals due to the free ligand $[\mathbf{L^{3S}}+2H]^-$ (m/z = 496.0) and $[\mathbf{L^{3S}}+3H+Cl]^-$ (m/z = 532.1). The $Ni_2\mathbf{L^{3S}}$ complex is detected only in excess of Ni^{II} with the anion $[Ni_2\mathbf{L^{3S}} - 2H]^-$ (m/z = 607.9) (Figure S2).

Overall, these data acquired at pH 7.4 evidence that, up to 1 Ni^{II} equiv., only one species is formed, corresponding to a mononuclear complex with a 1:1 stoichiometry. Considering the large molar absorption coefficient of the S^- to Ni^{II} LMCT bands and based on the following NMR and XAS spectroscopic studies, this complex is proposed to contain three S-donor atoms arising from the three cysteines and one O-donor atom arising from a water molecule (vide infra) in a square planar geometry: $[Ni\mathbf{L^{3S}}(OH_2)]^-$. The following experiments focus on the latter species, formed under slightly sub-stoichiometric conditions (Ni:$\mathbf{L^{3S}}$ 0.9:1) to fully avoid the formation of the 2:1 complex.

Evolution with pH. The pH effect on the speciation of the Ni^{II} complexes was investigated by UV-vis and CD spectroscopy from pH 4 to pH 11 by the successive addition of potassium hydroxide (KOH) into a water solution of Ni:$\mathbf{L^{3S}}$ 0.9:1 (Figure 3). The characteristic transitions previously identified for $Ni\mathbf{L^{3S}}(OH_2)$ at pH 7.4, at 289, 345 and 462 nm, are detected starting as low as pH 5.3. The maximum amount of this species is formed at pH 6.9. Above pH 7.5, the initial

species evolves exclusively into a second species, Ni**L**^{3S}(OH), as attested by the presence of three isobestic points at 290, 312 and 337 nm. The two LMCT bands are shifted to 270 nm (ε = 15 800 $M^{-1}cm^{-1}$) and 325 nm (ε = 8 600 $M^{-1}cm^{-1}$), and the d-d band to 483 nm (ε = 270 $M^{-1}cm^{-1}$). The formation of these two pH dependent species is confirmed by CD experiments (Figure S3). Between pH 7.0 and 11.0, the evolution of the CD spectra leads to five isodichroic points with notable changes between the spectra recorded at pH 7.1 and that at pH 10.6. ESI-MS was used to investigate the nuclearity of the second species, and the spectrum recorded at pH 9.5 in ammonium acetate buffer displays the same peak as observed at pH 6.9, corresponding to a 1:1 nuclearity (Ni:**L**^{3S}).

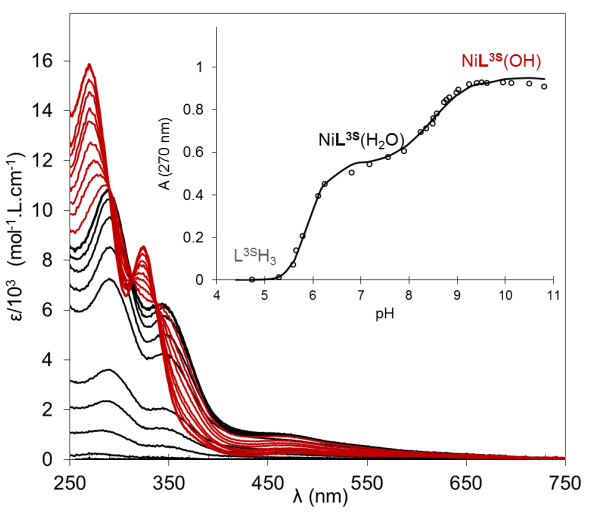

Figure 3. UV spectra of **L**^{3S} (72 μM) and 0.9 equiv. of Ni^{II} in water at different pH. Spectra recorded between pH 4 and 7.5 are shown in black, spectra recorded between pH 8 and 11 are shown in red. Inset: experimental (dots) and simulated (line) evolution of the absorbance at 270 nm with Specfit software, with $\log\beta_{110}$ = 14.6 and $\log\beta_{11\text{-}1}$ = 6.0.

The modeling of the effect of the pH on the intensity of the absorbance across the full UV-Vis spectral range has been carried out using SPECFIT software[64-66] (the evolution at 270 nm is depicted in the inset of Figure 3). Two deprotonation events are observed around pH 6.0 and pH 8.5, involving 3 and 1 proton(s), respectively. These data are consistent with the formation of Ni**L**^{3S}(OH_2), which requires the deprotonation of the three thiol functions of the cysteines with a corresponding $\log\beta_{110}$ value of 14.6. This high equilibrium constant value evidences the high stability of the complex; for comparison the Ni^{II} complexes with two successive cysteines –Cys-Cys- display one to three orders of magnitude lower affinity for Ni^{II} with $\log\beta_{110}$ = 12.2-13.5.[67] At higher pH, the second increase reflects another deprotonation assigned to the generation of a hydroxo ligand, leading to the Ni**L**^{3S}(OH) species. A p*K*a of 8.6 is thus experimentally determined for a Ni^{II}-bound water molecule in a square planar environment. This value is difficult to compare with literature data. Indeed, to the best of our knowledge, acidity constants for Ni^{II}-

bound water molecules are reported for six-coordinate Ni^{II} complexes only: for instance the experimental p*K*a value for $[Ni(OH_2)_6]^{2+}$ is 9.9.[68] The Ni^{II} species distribution profile with pH, depicted in Figure S4, shows that the major complex at physiological pH is Ni**L**^{3S}(OH_2) (> 97% at pH 7 and > 94% at pH 7.4), whereas Ni**L**^{3S}(OH) becomes predominant above pH 9.

Solution ^{1}H NMR investigation. The structures of both complexes have been investigated by ^{1}H NMR spectroscopy (Figures 4 and 5). Spectral characteristics of fully dissymmetric structures are expected because of the three cysteine units that are present in different environments due to the chirality of the ligand and the square-planar geometry of the complexes. Both spectra are characteristic of diamagnetic species (0-12 ppm), in agreement with a square planar geometry around a low spin Ni^{II} ion. Interestingly, the ^{1}H NMR spectra of the two complexes are drastically different: that of Ni**L**^{3S}(OH) displays well-resolved features, while that of Ni**L**^{3S}(OH_2) shows very broad peaks. This discrepancy suggests drastically different intra-molecular dynamics in the two complexes' coordination spheres.

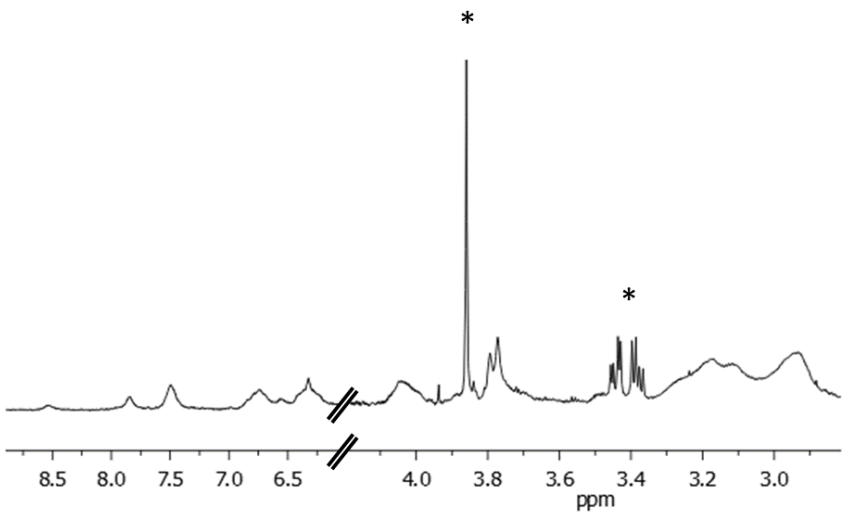

Figure 4. 500 MHz ^{1}H NMR of Ni**L**^{3S}(OH_2) 1.04 mM in H_2O/D_2O (90:10) at pH 7.2, 298 K, (*) 10% excess ligand. The complex was prepared *in situ* from $NiSO_4$ (1.04 mM) and **L**^{3S} (1.14 mM, 1.1 equiv.), the pH was increased to 7.2 with a KOH solution.

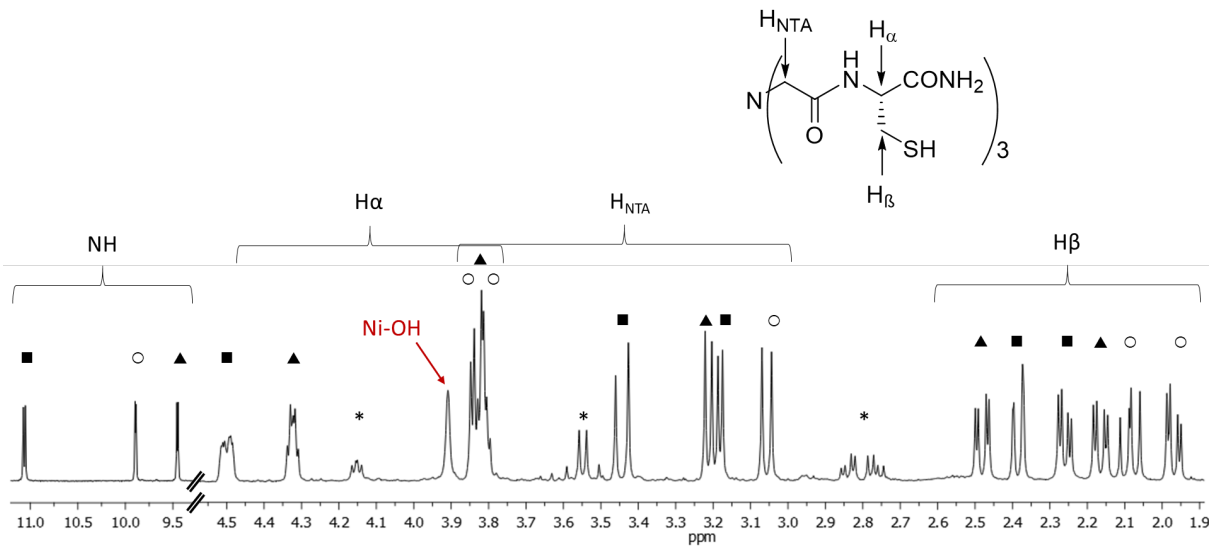

Figure 5. 500 MHz ^{1}H NMR of Ni**L^{3S}**(OH) 1.04 mM in H_2O/D_2O (90:10) at pH 10.1, 278 K. Each symbol corresponds to one of the three different arms of the ligand. (*) 10% excess ligand. A similar spectrum is obtained at 298 K, but one H_α is hidden by the water signal. The complex was prepared *in situ* from $NiSO_4$ (1.04 mM) and **L^{3S}** (1.14 mM, 1.1 equiv.), the pH was increased to 10.1 with a KOH solution.

The spectrum of Ni**L^{3S}**(OH) did not show significant evolution with temperature, from 278 K to 308 K, as seen in Figure S6. All peaks of the ^{1}H NMR spectrum at 278 K, recorded in light water at pH 10.1, have been attributed based on a detailed analysis of 2D-NMR experiments leading to structural information (Table S1). Whereas the primary amide NH_2 protons are not detected in light water, as expected for such a high pH, the NH protons of the 3 secondary amide functions are detected as narrow doublets. Indeed, these latter protons exhibit low temperature coefficients (between -1 and -3 ppb/K), characteristic of their involvement in intra-molecular hydrogen bond interactions.[69-70] This also confirms that the secondary amides are not deprotonated at pH 10.1, and therefore not coordinated to the Ni^{II} ion. Interestingly, the proton of the hydroxo ligand coordinated to the Ni^{II} ion has been detected as a large signal at 3.9 ppm, integrating for 1 proton, which disappears with D_2O addition. A strong NOE correlation in the 2D-NOESY spectrum indicates that this hydroxo proton is close to one of the Hβ protons from a cysteine (see NOESY in Figure S5). Besides, its temperature coefficient ($\delta\Delta/\Delta T$ = -3 ppb/K) also shows an intra-molecular hydrogen interaction. All of these interactions lead to an embedded environment around the Ni-OH unit allowing the observation of its ^{1}H NMR signal. The overall data confirm that at pH 10.1, the coordination sphere of the Ni^{II} ion is completed by the three thiolates of **L^{3S}** and a hydroxo ligand in a square planar geometry.

While the structure of Ni**L^{3S}**(OH) is dissymmetric and rigid, as attested by sharp and well resolved peaks, the ^{1}H NMR spectrum of Ni**L^{3S}**(OH_2) indicates that dynamic processes occur on the NMR timescale. The signals of Ni**L^{3S}**(OH_2) are very broad at room temperature and although

some of them are better resolved by lowering the temperature to 278 K, it was not possible to get a well-resolved spectrum for this complex (Figure S7). This is consistent with the presence of an exchangeable water molecule at pH 7.2 instead of a strongly coordinated hydroxo molecule at pH 10.1. The exchange of the Ni-bound water molecule between the 4 different positions accessible in the square-planar geometry and the intrinsic dissymmetry of the complex leads to a spectrum displaying unresolved and broad peaks that could not be investigated in more detail.

XAS characterization of the two complexes. Ni K-edge X-ray absorption spectroscopy (XAS) has been used to probe the local chemical, electronic, and structural environment of the Ni^{II} ion in Ni**L**^{3S}(OH_2) and Ni**L**^{3S}(OH). While the X-ray absorption near-edge structure (XANES) is informative regarding the geometry as well as the spin and oxidation state of the metal ion, the X-ray absorption fine structure (EXAFS) provides information about the coordination sphere and metal-ligand distances. The XAS spectra of Ni**L**^{3S}(OH_2) and Ni**L**^{3S}(OH) are very similar. The XANES spectra display a weak pre-edge transition at 8333 eV that is assigned to a Ni (1s→3d) transition (Figure 6).[71] Such a feature is formally dipole forbidden, but can gain intensity in non-centrosymmetric coordination environments through mixing between the 4p and 3d orbitals. An additional shoulder at 8338 eV is observed, attributed to a Ni (1s→$4p_z$) transition. Such transitions are only observed in complexes with four-coordinate planar or five-coordinate pyramidal geometries. The presence of both a weak pre-edge peak and a Ni (1s→$4p_z$) transition evidences a square planar geometry for both complexes Ni**L**^{3S}(OH_2) and Ni**L**^{3S}(OH).[71] The presence of more than two S-donor atoms in the coordination sphere of the Ni^{II} ion in Ni**L**^{3S}(OH_2) and Ni**L**^{3S}(OH) is proposed based on the comparison of their XANES spectra with that of a reference Ni complex with a N2S2 environment:[35] (i) the slopes of the edges for Ni**L**^{3S}(OH_2) and Ni**L**^{3S}(OH) are smaller than that of the Ni(N2S2) complex and (ii) their edges are shifted to a lower energy. Such observations are consistent with the fact that the presence of polarizable ligands such as thiolates decreases the positive charge density on the Ni^{II} ion.

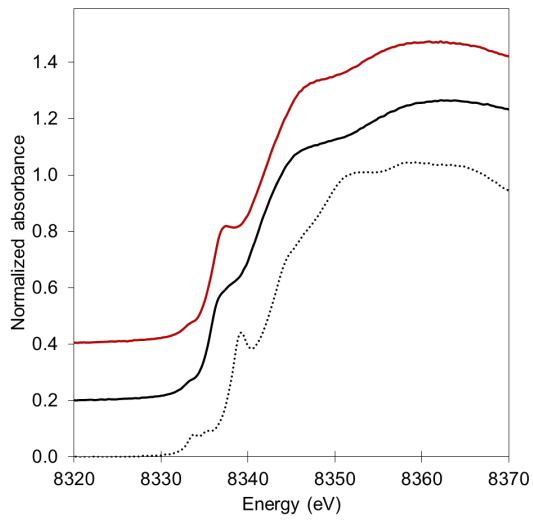

Figure 6. XANES spectra of Ni**L**^{3S}(OH_2) (black line, offset of 0.2), Ni**L**^{3S}(OH) (red line, offset of 0.4) and Ni(N2S2) (dashed line, offset of 0.0)

The best fit for the EXAFS region of the XAS spectrum of Ni**L**^{3S}(OH_2) uses a four coordinate model with the Ni center coordinated by three S-scatterers at 2.22 Å and one N/O-scatterer at 1.98 Å. Fits are presented in Figure 7 and Table 1. *CN* were initially not fixed with their sum equal to 4, and then fixed to the closest integers 3S/1O and 2S/2O (see Figure S8 for best fits with unfixed *CN*). Regarding Ni**L**^{3S}(OH), the best fit leads to three Ni-S scatterers at 2.21 Å and one Ni-N/O scatterer at 1.94 Å. Even if the EXAFS data are comparable for both complexes, the slight decrease of the Ni-(N/O) distance between Ni**L**^{3S}(OH_2) and Ni**L**^{3S}(OH) is consistent with the deprotonation of a water molecule since the Ni-O_{aquo} and Ni-$O_{hydroxo}$ distances are expected to be about 2.08 Å and 1.89 Å, respectively.[72-73]

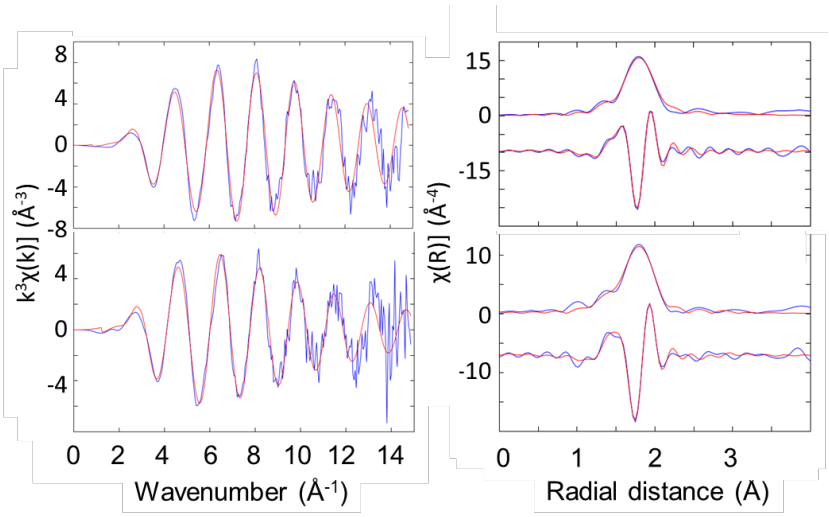

Figure 7. XAS data for Ni**L**^{3S}(OH_2) (top) and Ni**L**^{3S}(OH) (bottom) obtained on frozen solutions of 1.0 mM of complex at pH 7.5 and 9.6, respectively in water/glycerol (80:20). Left: k^3–weighted EXAFS data. Right: real and imaginary parts of the Fourier transforms of the k^3-weighted EXAFS

data. Experimental data in blue lines and fitted data in red lines (parameters used for the fit are those of Table 1 with fixed *CN*s).

Table 1. Structural parameters derived from Ni K-edge EXAFS analysis.

	Ni-S			**Ni-O/N**			**ΔE_0 (eV)**	**Res (%)**	**χ^2**
	R (Å)	*CN*	$\sigma^2.10^3$(Å^2)	*R* (Å)	*CN*	$\sigma^2.10^3$ (Å^2)			
NiL^{3S}(OH$_2$)	2.22(1)	2.8(8)[a]	1(1)[c]	1.99(1)	1.2(8)[a]	1(1)[c]	3(3)	1.2	173
NiL^{3S}(OH)	2.21(1)	2.7(3)[a]	3(1)	1.95(2)	1.3(3)[a]	7(4)	7(2)	0.9	92
NiL^{3S}(OH$_2$)	2.22(1)	3[b]	1(1)[c]	1.98(2)	1[b]	1(1)[c]	2.6(7)	1.2	143
NiL^{3S}(OH)	2.21(1)	3[b]	4(1)	1.94(2)	1[b]	7 (4)	5.9(9)	0.8	84
NiL^{3S}(OH$_2$)	2.24(1)	2	0.0(4)[c]	2.01(1)	2	0.0(4)[c]	7(1)	1.3	163
NiL^{3S}(OH)	2.24(1)	2	2.0(9)	1.99(2)	2	4(2)	12(2)	1.8	166

Experimental errors on the last character are indicated in parentheses. [a] Sum of *CNs* was fixed to 4. [b] Fixed *CN* value. [c] σ^2 values were set to be equal. Res = $[\Sigma(\chi_{exp} - \chi_{fit})^2/\Sigma(\chi_{exp})^2] \times 100$. χ^2 : fitting metric normalized by the degrees of freedom in the fit.

Theoretical calculations. To validate the proposed structures of Ni**L^{3S}**(OH$_2$) and Ni**L^{3S}**(OH) based on spectroscopic investigation, DFT and TD-DFT calculations have been carried out. Both optimized structures run in singlet state support a square planar geometry around the Ni^{II} ion, which is coordinated to the three thiolates arising from the cysteine arms and one oxygen atom coming from either a water or a hydroxo molecule in Ni**L^{3S}**(OH$_2$) or Ni**L^{3S}**(OH), respectively. The Ni-S bond lengths are in the normal range for Ni-S (2.20 to 2.28 Å), and the expected decrease of the Ni-O distance is observed when the hydroxo ligand replaces the water ligand (2.01 and 1.88Å, see Figure S9 and Table S2 for more details). These structural data are fully consistent with the EXAFS data.

In agreement with the NMR and XANES data, only the singlet state leads to a true energy minimum checked with all real frequencies (see computational details in SI). The TD-DFT predicted UV-vis properties of both complexes are consistent with the experimental data. The two main transitions experimentally observed at around 300 nm and 340 nm are calculated at 295 nm and 343 nm for Ni**L^{3S}**(OH$_2$). In the case of Ni**L^{3S}**(OH), the experimental shifts to higher energies of both transitions are also well reproduced at 272 nm and 323 nm (see Figure S13). An analysis of these transitions confirmed their LMCT nature, being mainly S (p orbitals) to Ni ($d_{x^2-y^2}$) excitations.

Redox properties of Ni**L**^{3S}(OH_2) **and** Ni**L**^{3S}(OH)**.** The cyclic voltammograms (CVs) of Ni**L**^{3S}(OH_2) and Ni**L**^{3S}(OH) have been recorded in HEPES solutions buffered at pH 7.4 and 9.5, respectively (Figure 8). The CV of Ni**L**^{3S}(OH_2) displays only one irreversible oxidation process at E_{pa} = 0.48 V vs SCE that can be attributed to the oxidation of Ni^{II} into Ni^{III}. The CV of Ni**L**^{3S}(OH) reveals the presence of two irreversible oxidation processes at E_{pa} = 0.31 V and E_{pa} = 0.59 V vs SCE. Since it is expected that the exchange of a water by a hydroxo ligand should decrease the oxidation potential of the Ni^{II} ion (charge effect), the first redox system is assigned to $Ni^{II} \rightarrow Ni^{III}$. Furthermore, the current intensity of this irreversible oxidation was compared with the reversible reduction of the redox probe $Ru^{III}(NH_3)_6Cl_3$ in HEPES. Similar current intensity for this system corroborates the monoelectronic nature of the oxidation of both Ni**L**^{3S}(OH_2) and Ni**L**^{3S}(OH). The second redox system is consistent with the oxidation of the ligand (see the CV of the ligand in Figure S10). Because the first oxidation is irreversible at all scan rates in the range 10 $mV.S^{-1}$ – 1 $V.s^{-1}$, the Ni^{III} species is unstable and it can be proposed that its degradation releases the ligand into the solution. Interestingly, the anodic potentials to oxidize both complexes are in an appropriate redox range to achieve SOD activity ($E_{ox}(O_2^{\bullet -})$ = -0.2 V; $E_{red}(O_2^{\bullet -})$ = 0.85 V vs SCE).

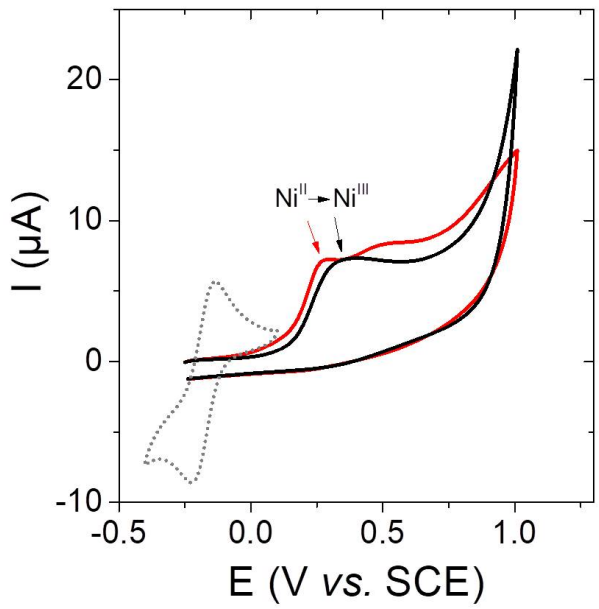

Figure 8. Cyclic voltammograms at 100 mV/s of Ni**L**^{3S}(OH_2) (black) and Ni**L**^{3S} (OH) (red) at 570 μM in Hepes buffer (20 mM, pH 7.4 and 9.5 respectively, [NaCl] = 100 mM), (dotted gray) CV at 100 mV/s of the $Ru^{III}(NH_3)_6Cl_3$ probe

SOD activity. The SOD activity of both complexes has been first evaluated based on the xanthine/xanthine oxidase system. In this assay, superoxide is produced constantly by the

enzyme and reacts with the *para*-nitro blue tetrazolium chloride (NBT) to generate the blue pigment formazan ($\lambda_{max} \approx 560$ nm (~35 000 $M^{-1}cm^{-1}$)). On the other hand, when a SOD catalyst is added to the system, the generation of formazan decreases because the catalyst prevents the oxidation of NBT by $O_2^{\bullet-}$ through its consumption (Scheme S1). An IC_{50} of about 1 μM has been measured at pH 7.4 for Ni**L**^{3S}(OH_2) (Figure S11), which represents 93% of the Ni^{II} species in these conditions. For comparison, controls with the ligand or the Ni^{II} salt alone showed no activity (See Figure S12B and C). The catalytic activity of Ni**L**^{3S}(OH_2) is similar to that reported for peptide-based nickel models,[44] but lower than the one reported for CuZn-SOD (4 10^{-8} M). However, the IC_{50} is larger than 100 μM at pH 9.6, where Ni**L**^{3S}(OH) is the major Ni^{II} species (92%). Although the structures of the two complexes only differ in their coordination by the presence of a water molecule or a hydroxo anion, only the Ni**L**^{3S}(OH_2) displays SOD activity.

To confirm these data, stopped-flow experiments have been conducted, where superoxide in DMSO is mixed with an aqueous solution of the complex. In this method, the consumption of superoxide is monitored by UV-vis spectroscopy under catalytic conditions. Without any catalyst, the self-disproportionation of superoxide follows a second order rate law. When an SOD-active molecule is added, the reaction rate becomes pseudo first order. For such measurements, high pH (around pH 8) should be preferred to slow down the $O_2^{\bullet-}$ self-disproportionation reaction. However, since the NBT/formazan assay evidences a better activity for Ni**L**^{3S}(OH_2), the activity has been tested at pH 7.75, where the ratio between Ni**L**^{3S}(OH_2) / Ni**L**^{3S}(OH) is about (86:14). Under these conditions, the rate constant for the superoxide self-disproportionation reaction was found to be k_{cat} = 3(1) 10^4 $M^{-1}s^{-1}$. As expected, the reaction between $O_2^{\bullet-}$ and Ni**L**^{3S}(OH_2) is faster than the self-disproportionation reaction and follows a first order rate law (Figure 9). The experiments have been done at different concentrations to determine the rate constant, k_{cat} = 1.8 10^5 $M^{-1}s^{-1}$. Even though the reaction is much faster between $O_2^{\bullet-}$ and Ni-SOD at pH 8 (k_{cat} ~ 1 10^9 $M^{-1}s^{-1}$),[74] it is the first nickel complex displaying activity under catalytic conditions with a coordination that notably differs from that of the enzyme, i.e. with no N-based donor ligand (S3O *vs* S2N2). Ni**L**^{3S}(OH_2) also displays a sulfur rich environment, a specific originality of the NiSOD with respect to the other SOD enzymes, evidencing the key role of the cysteines in the environment of the Ni ion. Interestingly, the absorption of the solution at 289 nm is similar before and after the catalysis suggesting that Ni**L**^{3S}(OH_2) is robust under catalytic conditions.

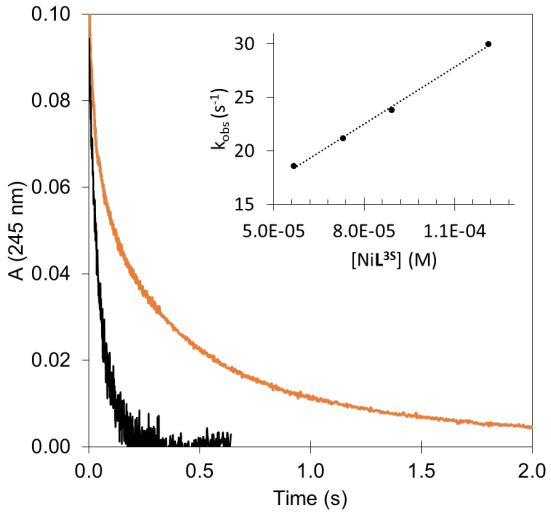

Figure 9. Disproportionation of $O_2^{\bullet-}$ (767 μM), self-disproportionation (orange line), and with 57 μM Ni**L**^{3S} (black line) in Hepes buffer (60 mM, pH 7.75, [NaCl] = 100 mM) and DMSO (5:1 ratio). Inset. Experimental k_{obs} as a function of the concentration of Ni**L**^{3S}.

Discussion.

Currently, only bio-inspired peptide-based SOD complexes display catalytic SOD reactivity,[17-26] while the low-molecular weight synthetic Ni^{II} complexes are not active as catalysts,[28-42] even if they can react with $O_2^{\bullet-}$, and despite efforts made to reproduce the key structural elements of the active site of the Ni-SOD. In this context, recent studies report on complexes with coordination spheres that deviate from an exact mimicry with the aim of probing the different mechanisms that can be involved and determining structure/activity correlations. Here, we proposed an original approach based on a pseudo-peptide ligand that leads to square-planar Ni complexes without N-donor atom in the Ni coordination sphere, but instead, an aquo or hydroxo ligand not present in the active site of the Ni-SOD.

The characterization of the two planar S3O Ni^{II} complexes [Ni**L**^{3S}(OH_2)]$^-$ (Ni**L**^{3S}(OH_2)) and [Ni**L**^{3S}(OH)]$^{2-}$ (Ni**L**^{3S}(OH)) has revealed that the ratio of these two species is pH dependent in aqueous solutions with a p*K*a of 8.6 for the water molecule bound to the Ni site. The pH speciation also shows that at physiological pH, the three sulphur atoms bound to the Ni^{II} ion belong to deprotonated thiolate functions from the cysteine residues. Therefore, in the SOD-active complex Ni**L**^{3S}(OH_2), the cysteine moieties are not protonated. This conclusion is in contrast to that arising from an investigation carried out on metallopeptide based models for which it has been proposed that protonation of one of the cysteines occurs during the catalytic mechanism.[26] However, this is perfectly consistent with a more recent study performed on similar maquettes that evidences that the cysteine residues are not protonated.[75]

The SOD efficiency of Ni**L**^{3S}(OH_2) (IC_{50} ~ 1 10^{-6} M, pH 7.4) is lower than that of the NiSOD (IC_{50} = 4-8 10^{-8} M per metallic site),[16] and the reaction is slower (k_{cat} = 1.8 10^5 $M^{-1}s^{-1}$, pH 7.75) than that between $O_2^{\bullet-}$ and NiSOD (k_{cat} ~ 1 10^9 $M^{-1}s^{-1}$, pH 6.0-8.0)[16] or peptide-based models (in the range 6 10^6 - 6 10^8 M^{-1} s^{-1}, pH 8.0). However, the activity of the present Ni^{II} SOD catalyst is expected to be enhanced at physiological pH, since the measured SOD activity at pH 7.75 contains a significant contribution of the inactive Ni**L**^{3S}(OH) complex. Unfortunately, since $O_2^{\bullet-}$ dismutation was revealed to be too fast at pH 7.4 to generate reproducible data, the activity at physiological pH, where Ni**L**^{3S}(OH_2) is exclusively present, cannot be measured.

The spectroscopic properties of both complexes highlight that the lability of the aquo and hydroxo ligands are notably different. In Ni**L**^{3S}(OH_2), the water molecule is labile as demonstrating by the broadening of the ^{1}H NMR resonances, reflecting the dynamics of the complex, while in Ni**L**^{3S}(OH), the structure is frozen, as attested by the observation of sharp ^{1}H NMR peaks and of the hydroxo proton, consistent with a non-labile hydroxo ligand. Interestingly, this difference of lability between the aquo and hydroxo ligands is correlated with the SOD activity of the complexes, with Ni**L**^{3S}(OH_2) being the much more active species. Because the redox potentials of the Ni^{II}/Ni^{III} couple in both species are compatible with SOD activity, this difference in reactivity provides insight into the mechanism. It suggests that a labile ligand (water molecule in this case) is required to carry out efficient SOD activity. Consequently, this supports the fact that $O_2^{\bullet-}$ should react with the Ni complex through its direct coordination, resulting in an inner sphere mechanism at least for one of the two reactions. Even though the Ni^{II}/Ni^{III} redox system is irreversible, SOD activity is observed. This suggests that the Ni^{III} species is unstable and quickly reacts with $O_2^{\bullet-}$, in favor of an outer sphere mechanism for the oxidation of $O_2^{\bullet-}$ into O_2. Consequently, we can propose that the reduction of $O_2^{\bullet-}$ occurs via an inner sphere mechanism. This result also shows that the reversibility of the Ni^{II}/Ni^{III} redox system, i.e. the generation of a stable Ni^{III} complex, is not a mandatory criterion for SOD activity under catalytic conditions.

Conclusion.

Through an original approach based on the use of pseudo-peptide ligands, we described here the first bio-inspired, low-molecular weight, synthetic Ni^{II} complex that displays catalytic SOD activity. Despite the fact that the coordination sphere of Ni**L**^{3S}(OH_2) strongly differs from that of the NiSOD (S3O *vs* N2S2), Ni**L**^{3S}(OH_2) is active in water at physiological pH. This is rationalized by the fact that the redox potential of the Ni^{II}/Ni^{III} couple is appropriate to perform such $O_2^{\bullet-}$ disproportionation. Another key structural feature is the presence of a labile ligand in the

coordination sphere of the Ni^{II} ion that is essential for the activity, thus implying an inner sphere mechanism, at least for the first part of the catalytic SOD cycle generating H_2O_2.

Experimental section

The synthesis of **L^{3S}** was performed as previously published.[51]

Solutions preparation: For the preparation of all the aqueous solutions, ultrapure laboratory grade water that has been filtered and purified by reverse osmosis using Millipore MilliQ reverse-osmosis cartridge system (resistivity 18MΩ cm) (Millipore) was used.
In order to prevent the oxidation of the cysteine residues, all the solutions were prepared under an argon atmosphere in a glovebox. Solutions of ligands or complexes were freshly prepared before each experiment in the appropriate deoxygenated buffer.
Ni^{II} solutions were prepared from the sulfate corresponding salt dissolved in water.
The ligand concentration for the different solutions was determined by the Ellman's procedure.[76] 5,5-dithiobis(2-nitrobenzoic acid) (DTNB) is used as an indicator. Each free thiol group present in the ligand yields 1 equiv. of TNB^{2-} [λ = 412 nm, $\varepsilon(TNB^{2-})$ = 14150 M^{-1} cm^{-1}].
For the complex solutions, 0.9 equiv. of Ni^{II} were added to the ligand in the proper buffer so that only the mononuclear complex is formed.

UV and CD spectroscopy: The UV spectra were recorded with a Varian Cary50 spectrophotometer equipped with optical fibers connected to an external cell holder in a glovebox. The circular dichroism spectra were acquired with an Applied Photophysics Chirascan spectrometer. Spectra were recorded in the 230–630 nm wavelength range with 1 nm bandwidth and 1 second dwell time per point. For each sample, 2 parallel spectra were recorded and the average of these spectra was smoothed by the Savitzky– Golay method with a ''window size'' 7. CD spectra are reported in molar ellipticity [Θ] defined as [Θ] = $\theta_{obs}/(10lc)$ where θ_{obs} is the ellipticity in millidegrees, l the optical path length of the cell in centimeters and c the species concentration in moles per litre. Quartz cells with 1 cm pathlength were used.
For the ligand titration with Ni^{II}, 2.5 mL of a ligand solution (50-75 μM) in Hepes buffer (20 mM, pH 7.4, [NaCl] = 100 mM) were titrated with aliquots of the Ni^{II} solution. The UV-Vis and CD spectra were recorded after 10 min stabilization.
For the pH studies, 2.5 mL of a complex solution (50-75 μM) in water were titrated with aliquots of a 0.01 M KOH solution. The pH was measured using a Metrohm 702 SM Titrino equipped with a Mettler Toledo InLabs Micro-electrode. The UV-Vis and CD spectra were recorded after 10 min stabilization. These data were fitted with the SPECFIT program with fixed values for the pKa of

$\mathbf{L^{3S}}$ (pKa_1 = 10.2, pKa_2 = 9.2, pKa_3 = 8.5).[51] The best fit was obtained considering the two global constants β_{110} and $\beta_{11\text{-}1}$ defined as:

$Ni^{II} + \mathbf{L^{3S}} \leftrightarrows Ni\mathbf{L^{3S}}$ (β_{110})

$Ni^{II} + \mathbf{L^{3S}} \leftrightarrows Ni\mathbf{L^{3S}}H_{-1} + H^+$ ($\beta_{11\text{-}1}$)

$Ni\mathbf{L^{3S}} \leftrightarrows Ni\mathbf{L^{3S}}H_{-1} + H^+$ Ka ($Ni\mathbf{L^{3S}}/Ni\mathbf{L^{3S}}H_{-1}$) = $\beta_{11\text{-}1}/\beta_{110}$

Mass spectrometry: Mass spectra were acquired on a LXQ-linear ion trap (THERMO Scientific) instrument equipped with an electrospray ion source. Electrospray full scan spectra in the range of m/z = 50–2000 amu were obtained by infusion through a fused silica tubing at a flow rate of 2–10 mL/min. The solutions were analyzed in negative and positive ion modes. The LXQ calibration (m/z = 50–2000) was achieved according to the standard calibration procedure from the manufacturer (mixture of caffeine, MRFA and Ultramark 1621). The temperature of the heated capillary for the LXQ was set in the range of 200– 250°C, the ion-spray voltage was in the range of 3–6 kV and the injection time was 5–200 ms. The ligand solution (≈ 150 μM) was prepared in ammonium acetate buffer (20 mM, pH 6.9) and aliquots of Ni^{2+} were then added.

^{1}H NMR Spectroscopy: The NMR experiments were recorded on a 500 MHz Bruker Avance spectrometer equipped with a BBI probe with triple axis gradient field. Complex samples at ≈1 mM were prepared in H_2O/D_2O (v/v=9/1) and the pH was adjusted to 10.1 or 7.2 using a KOH solution. Spectra were acquired on a 15 ppm window and 32k data points in the time domain with a presaturation or a watergate pulse program to suppress the water signal. The temperature coefficients of the amide and the hydroxo protons were measured using watergate water suppression between 278 and 308 K.

Electrochemistry: Cyclic voltammograms were recorded with a Metrohm Autolab PGSTAT100 potentiostat at 100 mV/s. A glassy carbon electrode was used as the working electrode, a platinum wire as the auxiliary electrode and SCE as the reference. Solutions of $Ni\mathbf{L^{3S}}(OH_2)$ and $Ni\mathbf{L^{3S}}(OH)$ (570 μM) were prepared in Hepes buffer (20 mM, [NaCl] = 100 mM) at pH 7.4 and 9.5, respectively.

X-Ray Absorption Spectroscopy: Ni K-edge XANES (X-ray Absorption Near-Edge Structure) and EXAFS (Extended X-ray Absorption Fine Structure) spectra were recorded at the BM30B (FAME) beamline at the European synchrotron radiation facility (ESRF, Grenoble, France) using a Si(220) double-crystal monochromator.

The complexes were prepared at 1.0 mM in water/glycerol (80:20) in order to prevent ice crystallization. The pH was then adjusted with KOH to 7.5 or 9.6 to generate $Ni\mathbf{L^{3S}}(OH_2)$ and

Ni**L**^{3S}(OH). The complex solutions were placed in a sample holder with Kapton tape windows and flash-frozen in liquid nitrogen, and the frozen glass was mounted in a continuous flow helium-vapor cryostat (8 K ≤ T ≤ 20 K) to minimize sample photo-damage. Spectra were measured in fluorescence-yield detection mode with a 30-element Ge Canberra detector. At least nine scans were averaged for each samples. Data were acquired in 5 eV steps in the pre-edge region (8100-8295 eV), 0.25 eV steps in the edge region (8295 – 8375 eV), 2 eV steps in the post-edge region (8375 – 9182 eV). The energy was calibrated with a Ni metallic foil, such that the maximum of the first derivative was set at 8333 eV.

The data analyses were performed using the Demeter package, including ATHENA for the data extraction and ARTEMIS for the shell fitting.[77] The k^3-weighted EXAFS spectra were Fourier-transformed over the k range 2–13 $Å^{-1}$ using a Hanning window. The fits were performed on the Fourier-transformed spectra over the R range 1–2.4 Å. $Ni(H_2O)_6$, $Ni(cyclam)(CH_3CN)_2$,[78] $Ni(Acac)_2$ and NiS2N2[35] were used as reference complexes to determine the amplitude reduction factor S_0^2 which was averaged and set to 0.76. The aquo complex was prepared at 1 mM in water from $NiSO_4$, the other ones were analyzed as powder in BN pellets.

Xanthine/Xanthine Oxidase assay: The superoxide was generated with the Xanthine/Xanthine Oxidase system developed by Fridovich and Beauchamp,[79] and adapted by Tabbi *et al.*[80] In this test, the IC_{50} is defined as the SOD concentration needed to inhibit 50% of the NBT conversion to formazan.

In a typical experiment, xanthine oxidase is added to a solution (final volume of 2 mL) of 50 μM xanthine, 100 μM NBT in Hepes buffer (20 mM, pH 7.4 or 9.4, [NaCl] = 100 mM) in order to have an increase of the absorbance of ΔA_{560} = 0.024 min^{-1} before the addition of the complex. The reaction was monitored during 150 seconds or less to ensure a stationary state for the superoxide production. The IC_{50} is reached when the slope after the complex addition is ΔA_{560} = 0.012 min^{-1}.

To be sure that the complexes have no influence on the superoxide production, the formation of urate without NBT was also monitored at 290 nm in their absence and in their presence, no difference in the slope was observed.

KO_2 solution in DMSO: Fresh KO_2 solutions were prepared before each experiment by stirring vigorously ≈100 mg of solid KO_2 in 10 mL of dry DMSO. The solutions were filtered after 30 minutes (0.45 μM, PTFE) to give slightly yellow solutions and the superoxide concentration was determined by UV spectroscopy (0.2 mm length path cell, ε_{250} = 2686 $M^{-1}cm^{-1}$) and was typically ≈5 mM.

Stopped-flow: Stopped-flow experiments were performed at 25.0°C on a Biologic SFM-400 using the first three syringes and a high density mixer to minimize optical perturbations due to the mix of solvents. A J&M TIDAS diode array detector (integration time 0.8 ms) and a Hamamatsu L10290 light source were used. The first syringe was filled with Hepes buffer (60 mM, pH 7.75, [NaCl] = 100 mM), the second one with the complex in the same buffer, and the third one with KO_2 in DMSO. The ratio for the syringes was set to 5:5:2, respectively in order to have reproducible shots and an excess of superoxide (constant ratio of 5:1 buffer/DMSO). The dismutation of superoxide was monitored by measuring the absorbance at 245 nm during 2.2 s after the injection in the cell. At least 9 shots were averaged for each complex concentration (range 50-150 μM). Shots of the Ni^{II} complex at different concentrations without superoxide evidence that the complexes remain stable in DMSO containing solutions for the duration of the entire experiment. They were averaged and used as baselines. Data were processed using the Biokine software. No catalytic activity was observed in the control experiment with $NiSO_4$ (500 μM).

Computational details: Density Functional calculations in the Kohn-Sham approach have been carried out with Orca 3.0.3.[81] Geometry optimizations have been performed with the hybrid functional B3LYP to which the Grimme dispersion correction with Becke-Johnson damping (D3BJ)[82-83] has been added, and using the Alhrich def2-tzvp basis set[84-85] for all atoms. The RIJCOSX approximation[86-87] has been used for all calculations. Harmonic frequencies have been calculated at the same level to check the nature of the stationary points. Electronic transitions have been calculated through the TD-DFT module on 20 roots using the range-separated CAM-B3LYP.[88] The latter functional was shown to be the most adapted thanks to a benchmark on the UV spectrum of Ni$\mathbf{L^{3S}}$(OH_2) (see SI for details) including normal hybrids and range-separated ones. TightSCF criteria have been used in all calculations. Geometry optimizations, frequencies and TDDFT spectra, were performed with a solvent continuum (COSMO)[89] modeling the water solvent.

Supporting Information

ESI-MS spectra of the complexes, supplementary figures for CD, ^{1}H NMR, EXAFS, DFT, electrochemistry and xanthine oxidase assay. Comparison between TD DFT and experimental UV data. xyz coordinates in the optimized structures of the two complexes.

Corresponding Author

*email for C. D.: carole.duboc@univ-grenoble-alpes.fr , P. D.: pascale.delangle@cea.fr

Notes

The authors declare no competing financial interest.

Acknowledgements.

The authors gratefully acknowledge research support of this work by the French National Agency for Research in the framework of the "Investissements d'avenir" program (ANR-15-IDEX-02), the Labex ARCANE (ANR-11-LABX-003) and the CBH-EUR-GS (ANR-17-EURE-0003). Olivier Sénèque and Fabrice Thomas are acknowledged for their help to set-up the stopped-flow experiments. The authors acknowledge the CRG-SOLEIL program committees for provision of synchrotron radiation beamtime (proposal 20170141) and all the FAME beamline staff for his help during the experiment.

References.

1. Sheng, Y.; Abreu, I. A.; Cabelli, D. E.; Maroney, M. J.; Miller, A.-F.; Teixeira, M.; Valentine, J. S., Superoxide Dismutases and Superoxide Reductases. *Chem. Rev.* **2014,** *114*, 3854-3918.
2. Miller, A. F., Superoxide dismutases: active sites that save, but a protein that kills. *Curr. Opin. Chem. Biol.* **2004,** *8*, 162-168.
3. Tainer, J. A.; Getzoff, E. D.; Richardson, J. S.; Richardson, D. C., Structure and mechanism of copper, zinc superoxide dismutase. *Nature* **1983,** *306*, 284-287.
4. Grasbon-Frodl, E. M.; Kösel, S.; Riess, O.; Müller, U.; Mehraein, P.; Graeber, M. B., Analysis of Mitochondrial Targeting Sequence and Coding Region Polymorphisms of the Manganese Superoxide Dismutase Gene in German Parkinson Disease Patients. *Biochem. Biophys. Res. Commun.* **1999,** *255*, 749-752.
5. Grove, L. E.; Brunold, T. C., SECOND-SPHERE TUNING OF THE METAL ION REDUCTION POTENTIALS IN IRON AND MANGANESE SUPEROXIDE DISMUTASES. *Comments Inorg. Chem.* **2008,** *29*, 134-168.
6. Miller, A.-F., Redox Tuning over Almost 1 V in a Structurally Conserved Active Site: Lessons from Fe-Containing Superoxide Dismutase. *Acc. Chem. Res.* **2008,** *41*, 501-510.
7. Tierney, D. L.; Fee, J. A.; Ludwig, M. L.; Penner-Hahn, J. E., X-ray Absorption Spectroscopy of the Iron Site in Escherichia coli Fe(III) Superoxide Dismutase. *Biochemistry* **1995,** *34*, 1661-1668.
8. Grove, L. E.; Xie, J.; Yikilmaz, E.; Karapetyan, A.; Miller, A.-F.; Brunold, T. C., Spectroscopic and Computational Insights into Second-Sphere Amino-Acid Tuning of Substrate Analogue/Active-Site Interactions in Iron(III) Superoxide Dismutase. *Inorg. Chem.* **2008,** *47*, 3993-4004.
9. Robinett, N. G.; Peterson, R. L.; Culotta, V. C., Eukaryotic Cu-only superoxide dismutases (SODs): A new class of SOD enzymes and SOD-like protein domains. *J. Biol. Chem.* **2017**.
10. Youn, H.-D.; Kim, E.-J.; Roe, J.-H.; Hah, Y. C.; Kang, S.-O., A novel nickel-containing superoxide dismutase from Streptomyces spp. *Biochem. J.* **1996,** *318* 889-896.

11. Sigel, A.; Sigel, H.; Sigel, R. K. O., *Nickel and Its Surprising Impact in Nature.* John Wiley & Sons Ltd.: Chichester, UK, 2007; Vol. 2.
12. Grapperhaus, C. A.; Darensbourg, M. Y., Oxygen capture by sulfur in nickel thiolates. *Acc. Chem. Res.* **1998,** *31*, 451-459.
13. Kaasjager, V. E.; Bouwman, E.; Gorter, S.; Reedijk, J.; Grapperhaus, C. A.; Reibenspies, J. H.; Smee, J. J.; Darensbourg, M. Y.; Derecskei-Kovacs, A.; Thomson, L. M., Unique Reactivity of a Tetradentate N2S2 Complex of Nickel:â€‰ Intermediates in the Production of Sulfur Oxygenates. *Inorg. Chem.* **2002,** *41*, 1837-1844.
14. Barondeau, D. P.; Kassmann, C. J.; Bruns, C. K.; Tainer, J. A.; Getzoff, E. D., Nickel superoxide dismutase structure and mechanism. *Biochemistry* **2004,** *43*, 8038-8047.
15. Wuerges, J.; Lee, J.-W.; Yim, Y.-I.; Yim, H.-S.; Kang, S.-O.; Djinovic Carugo, K., Crystal structure of nickel-containing superoxide dismutase reveals another type of active site. *Proc. Natl. Acad. Sci. U.S.A.* **2004,** *101*, 8569-8574.
16. Choudhury, S. B.; Lee, J. W.; Davidson, G.; Yim, Y. I.; Bose, K.; Sharma, M. L.; Kang, S. O.; Cabelli, D. E.; Maroney, M. J., Examination of the nickel site structure and reaction mechanism in Streptomyces seoulensis superoxide dismutase. *Biochemistry* **1999,** *38*, 3744-3752.
17. Shearer, J.; Long, L. M., A Nickel Superoxide Dismutase Maquette That Reproduces the Spectroscopic and Functional Properties of the Metalloenzyme. *Inorg. Chem.* **2006,** *45*, 2358-2360.
18. Neupane, K. P.; Shearer, J., The influence of amine/amide versus bisamide coordination in nickel superoxide dismutase. *Inorg. Chem.* **2006,** *45*, 10552-10566.
19. Schmidt, M.; Zahn, S.; Carella, M.; Ohlenschlager, O.; Gorlach, M.; Kothe, E.; Weston, J., Solution structure of a functional biomimetic and mechanistic implications for nickel superoxide dismutases. *Chembiochem* **2008,** *9*, 2135-2146.
20. Tietze, D.; Breitzke, H.; Imhof, D.; Kothe, E.; Weston, J.; Buntkowsky, G., New Insight into the Mode of Action of Nickel Superoxide Dismutase by Investigating Metallopeptide Substrate Models. *Chem. Eur. J.* **2009,** *15*, 517-523.
21. Shearer, J.; Neupane, K. P.; Callan, P. E., Metallopeptide Based Mimics with Substituted Histidines Approximate a Key Hydrogen Bonding Network in the Metalloenzyme Nickel Superoxide Dismutase. *Inorg. Chem.* **2009,** *48*, 10560-10571.
22. Krause, M. E.; Glass, A. M.; Jackson, T. A.; Laurence, J. S., Novel Tripeptide Model of Nickel Superoxide Dismutase. *Inorg. Chem.* **2010,** *49*, 362-364.
23. Tietze, D.; Tischler, M.; Voigt, S.; Imhof, D.; Ohlenschlager, O.; Gorlach, M.; Buntkowsky, G., Development of a Functional cis-Prolyl Bond Biomimetic and Mechanistic Implications for Nickel Superoxide Dismutase. *Chem. Eur. J.* **2010,** *16*, 7572-7578.
24. Krause, M. E.; Glass, A. M.; Jackson, T. A.; Laurence, J. S., MAPping the Chiral Inversion and Structural Transformation of a Metal-Tripeptide Complex Having Ni-Superoxide Dismutase Activity. *Inorg. Chem.* **2011,** *50*, 2479-2487.
25. Tietze, D.; Voigt, S.; Mollenhauer, D.; Tischler, M.; Imhof, D.; Gutmann, T.; Gonzalez, L.; Ohlenschlager, O.; Breitzke, H.; Gorlach, M.; Buntkowsky, G., Revealing the Position of the Substrate in Nickel Superoxide Dismutase: A Model Study. *Angew. Chem. Int. Ed.* **2011,** *50*, 2946-2950.
26. Shearer, J.; Peck, K. L.; Schmitt, J. C.; Neupane, K. P., Cysteinate Protonation and Water Hydrogen Bonding at the Active-Site of a Nickel Superoxide Dismutase Metallopeptide-Based Mimic: Implications for the Mechanism of Superoxide Reduction. *J. Am. Chem. Soc.* **2014,** *136*, 16009-16022.

27. Broering, E. P.; Truong, P. T.; Gale, E. M.; Harrop, T. C., Synthetic Analogues of Nickel Superoxide Dismutase: A New Role for Nickel in Biology. *Biochemistry* **2013,** *52*, 4-18.
28. Shearer, J.; Zhao, N., [Me4N](NiII(BEAAM)): A Synthetic Model for Nickel Superoxide Dismutase That Contains Ni in a Mixed Amine/Amide Coordination Environment. *Inorg. Chem.* **2006,** *45*, 9637-9639.
29. Mullins, C. S.; Grapperhaus, C. A.; Frye, B. C.; Wood, L. H.; Hay, A. J.; Buchanan, R. M.; Mashuta, M. S., Synthesis and Sulfur Oxygenation of a (N3S)Ni Complex Related to Nickel-Containing Superoxide Dismutase. *Inorg. Chem.* **2009,** *48*, 9974-9976.
30. Jenkins, R. M.; Singleton, M. L.; Almaraz, E.; Reibenspies, J. H.; Darensbourg, M. Y., Imidazole-Containing (N3S)-NiII Complexes Relating to Nickel Containing Biomolecules. *Inorg. Chem.* **2009,** *48*, 7280-7293.
31. Gale, E. M.; Patra, A. K.; Harrop, T. C., Versatile Methodology Toward NiN2S2 Complexes as Nickel Superoxide Dismutase Models: Structure and Proton Affinity. *Inorg. Chem.* **2009,** *48*, 5620-5622.
32. Ma, H. B.; Wang, G. B.; Yee, G. T.; Petersen, J. L.; Jensen, M. P., Scorpionate-supported models of nickel-dependent superoxide dismutase. *Inorg. Chim. Acta* **2009,** *362*, 4563-4569.
33. Gale, E. M.; Narendrapurapu, B. S.; Simmonett, A. C.; Schaefer, H. F.; Harrop, T. C., Exploring the Effects of H-Bonding in Synthetic Analogues of Nickel Superoxide Dismutase (Ni-SOD): Experimental and Theoretical Implications for Protection of the Ni-SCys Bond. *Inorg. Chem.* **2010,** *49*, 7080-7096.
34. Mathrubootham, V.; Thomas, J.; Staples, R.; McCraken, J.; Shearer, J.; Hegg, E. L., Bisamidate and Mixed Amine/Amidate NiN2S2 Complexes as Models for Nickel-Containing Acetyl Coenzyme A Synthase and Superoxide Dismutase: An Experimental and Computational Study. *Inorg. Chem.* **2010,** *49*, 5393-5406.
35. Gennari, M.; Orio, M.; Pécaut, J.; Neese, F.; Collomb, M.-N.; Duboc, C., Reversible Apical Coordination of Imidazole between the Ni(III) and Ni(II) Oxidation States of a Dithiolate Complex: A Process Related to the Ni Superoxide Dismutase. *Inorg. Chem.* **2010,** *49*, 6399-6401.
36. Gale, E. M.; Simmonett, A. C.; Telser, J.; Schaefer, H. F.; Harrop, T. C., Toward Functional Ni-SOD Biomimetics: Achieving a Structural/Electronic Correlation with Redox Dynamics. *Inorg. Chem.* **2011,** *50*, 9216-9218.
37. Gale, E. M.; Cowart, D. M.; Scott, R. A.; Harrop, T. C., Dipeptide-Based Models of Nickel Superoxide Dismutase: Solvent Effects Highlight a Critical Role to Ni–S Bonding and Active Site Stabilization. *Inorg. Chem.* **2011,** *50*, 10460-10471.
38. Herdt, D. R.; Grapperhaus, C. A., Kinetic study of nickel-thiolate oxygenation by hydrogen peroxide. Implications for nickel-containing superoxide dismutase. *Dalton Trans.* **2012,** *41*, 364-366.
39. Lee, W. Z.; Chiang, C. W.; Lin, T. H.; Kuo, T. S., A Discrete Five-Coordinate NiIII Complex Resembling the Active Site of the Oxidized Form of Nickel Superoxide Dismutase. *Chem. Eur. J.* **2012,** *18*, 50-53.
40. Nakane, D.; Wasada-Tsutsui, Y.; Funahashi, Y.; Hatanaka, T.; Ozawa, T.; Masuda, H., A Novel Square-Planar Ni(II) Complex with an Amino—Carboxamido—Dithiolato-Type Ligand as an Active-Site Model of NiSOD. *Inorg. Chem.* **2014,** *53*, 6512-6523.
41. Chiang, C.-W.; Chu, Y.-L.; Chen, H.-L.; Kuo, T.-S.; Lee, W.-Z., Synthesis and Characterization of NiIIIN3S2 Complexes as Active Site Models for the Oxidized Form of Nickel Superoxide Dismutase. *Chem. Eur. J.* **2014,** *20*, 6283-6286.

42. Broering, E. P.; Dillon, S.; Gale, E. M.; Steiner, R. A.; Telser, J.; Brunold, T. C.; Harrop, T. C., Accessing Ni(III)-Thiolate Versus Ni(II)-Thiyl Bonding in a Family of Ni–N2S2 Synthetic Models of NiSOD. *Inorg. Chem.* **2015,** *54*, 3815-3828.
43. Shearer, J., Insight into the Structure and Mechanism of Nickel-Containing Superoxide Dismutase Derived from Peptide-Based Mimics. *Acc. Chem. Res.* **2014,** *47*, 2332-2341.
44. Neupane, K. P.; Gearty, K.; Francis, A.; Shearer, J., Probing variable axial ligation in nickel superoxide dismutase utilizing metal lopeptide-based models: Insight into the superoxide disproportionation mechanism. *J. Am. Chem. Soc.* **2007,** *129*, 14605-14618.
45. Tietze, D.; Sartorius, J.; Seth, B. K.; Herr, K.; Heimer, P.; Imhof, D.; Mollenhauer, D.; Buntkowsky, G., New insights into the mechanism of nickel superoxide degradation from studies of model peptides. *Sci. Rep.* **2017,** *7*.
46. Truong, P. T.; Gale, E. M.; Dzul, S. P.; Stemmler, T. L.; Harrop, T. C., Steric Enforcement about One Thiolate Donor Leads to New Oxidation Chemistry in a NiSOD Model Complex. *Inorg. Chem.* **2017,** *56*, 7761-7780.
47. Huang, H.-T.; Dillon, S.; Ryan, K. C.; Campecino, J. O.; Watkins, O. E.; Cabelli, D. E.; Brunold, T. C.; Maroney, M. J., The Role of Mixed Amine/Amide Ligation in Nickel Superoxide Dismutase. *Inorg. Chem.* **2018,** *57*, 12521-12535.
48. Chatterjee, S. K.; Maji, R. C.; Barman, S. K.; Olmstead, M. M.; Patra, A. K., Hexacoordinate Nickel(II)/(III) Complexes that Mimic the Catalytic Cycle of Nickel Superoxide Dismutase. *Angew. Chem. Int. Ed.* **2014,** *53*, 10184-10189.
49. Truong, P. T.; Broering, E. P.; Dzul, S. P.; Chakraborty, I.; Stemmler, T. L.; Harrop, T. C., Simultaneous nitrosylation and N-nitrosation of a Ni-thiolate model complex of Ni-containing SOD. *Chem. Sci.* **2018,** *9*, 8567-8574.
50. Pujol, A. M.; Gateau, C.; Lebrun, C.; Delangle, P., A Cysteine-Based Tripodal Chelator with a High Affinity and Selectivity for Copper(I). *J. Am. Chem. Soc.* **2009,** *131*, 6928-6929.
51. Pujol, A. M.; Gateau, C.; Lebrun, C.; Delangle, P., A Series of Tripodal Cysteine Derivatives as Water-Soluble Chelators that are Highly Selective for Copper(I). *Chem. Eur. J.* **2011,** *17*, 4418-4428.
52. Pujol, A. M.; Lebrun, C.; Gateau, C.; Manceau, A.; Delangle, P., Mercury-Sequestering Pseudopeptides with a Tris(cysteine) Environment in Water. *Eur. J. Inorg. Chem.* **2012**, 3835-3843.
53. Jullien, A. S.; Gateau, C.; Lebrun, C.; Delangle, P., Mercury Complexes with Tripodal Pseudopeptides Derived from D-Penicillamine Favour a HgS3 Coordination. *Eur. J. Inorg. Chem.* **2015**, 3674-3680.
54. Jullien, A. S.; Gateau, C.; Lebrun, C.; Kieffer, I.; Testemale, D.; Delangle, P., D-Penicillamine Tripodal Derivatives as Efficient Copper(I) Chelators. *Inorg. Chem.* **2014,** *53*, 5229-5239.
55. Jullien, A. S.; Gateau, C.; Lebrun, C.; Delangle, P., Pseudo-peptides Based on Methyl Cysteine or Methionine Inspired from Mets Motifs Found in the Copper Transporter Ctr1. *Inorg. Chem.* **2015,** *54*, 2339-2344.
56. Jullien, A. S.; Gateau, C.; Kieffer, I.; Testemale, D.; Delangle, P., X-ray Absorption Spectroscopy Proves the Trigonal-Planar Sulfur-Only Coordination of Copper(I) with High-Affinity Tripodal Pseudopeptides. *Inorg. Chem.* **2013,** *52*, 9954-9961.
57. Pujol, A. M.; Cuillel, M.; Jullien, A. S.; Lebrun, C.; Cassio, D.; Mintz, E.; Gateau, C.; Delangle, P., A Sulfur Tripod Glycoconjugate that Releases a High-Affinity Copper Chelator in Hepatocytes. *Angew. Chem. Int. Ed.* **2012,** *51*, 7445-7448.

58. Conte-Daban, A.; Boff, B.; Matias, A. C.; Aparicio, C. N. M.; Gateau, C.; Lebrun, C.; Cerchiaro, G.; Kieffer, I.; Sayen, S.; Guillon, E.; Delangle, P.; Hureau, C., A Trishistidine Pseudopeptide with Ability to Remove Both Cu-I and Cu-II from the Amyloid-beta Peptide and to Stop the Associated ROS Formation. *Chem. Eur. J.* **2017,** *23*, 17078-17088.
59. Stetson, N. T.; Kauzlarich, S. M., A new material with alternating metal-oxide and metal-phosphide layers: barium manganese phosphate (Ba2Mn3P2O2). *Inorg. Chem.* **1991,** *30*, 3969-3971.
60. Stibrany, R. T.; Fox, S.; Bharadwaj, P. K.; Schugar, H. J.; Potenza, J. A., Structural and Spectroscopic Features of Mono- and Binuclear Nickel(II) Complexes with Tetradentate N(amine)2S(thiolate)2 Ligation. *Inorg. Chem.* **2005,** *44*, 8234-8242.
61. Cotton, F. A.; Wilkinson, G., *Advanced Inorganic Chemistry, 5th edition*. Wiley: New-York, 1999.
62. Kozlowski, H.; Révérend, B. D.-L.; Ficheux, D.; Loucheux, C.; Sovago, I., Nickel(II) complexes with sulfhydryl containing peptides. potentiometric and spectroscopic studies. *J. Inorg. Biochem.* **1987,** *29*, 187-197.
63. Chang, J. W.; Martin, R. B., Visible circular dichroism of planar nickel ion complexes of peptides and cysteine and derivatives. *J. Phys. Chem.* **1969,** *73*, 4277-4283.
64. Gampp, H.; Maeder, M.; Meyer, C. J.; Zuberbu¨hler, A. D., Calculation of equilibrium constants from multiwavelength spectroscopic data—II132, 95.: Specfit: two user-friendly programs in basic and standard fortran 77. *Talanta* **1985,** *32*, 257-264.
65. Gampp, H.; Maeder, M.; Meyer, C. J.; Zuberbühler, A. D., Calculation of equilibrium constants from multiwavelength spectroscopic data—III: Model-free analysis of spectrophotometric and ESR titrations. *Talanta* **1985,** *32*, 1133-1139.
66. Gampp, H.; Maeder, M.; Meyer, C. J.; Zuberbühler, A. D., Calculation of equilibrium constants from multiwavelength spectroscopic data—I: Mathematical considerations. *Talanta* **1985,** *32*, 95-101.
67. Rowinska-Zyrek, M.; Witkowska, D.; Bielinska, S.; Kamysz, W.; Kozlowski, H., The –Cys–Cys– motif in Helicobacter pylori's Hpn and HspA proteins is an essential anchoring site for metal ions. *Dalton Trans.* **2011,** *40*, 5604-5610.
68. Gilson, R.; Durrant, M. C., Estimation of the pKa values of water ligands in transition metal complexes using density functional theory with polarized continuum model solvent corrections. *Dalton Trans.* **2009**, 10223-10230.
69. Cierpicki, T.; Otlewski, J., *J. Biomol. NMR* **2001,** *21*, 249-261.
70. Baxter, N. J.; Williamson, M. P., *J. Biomol. NMR* **1997,** *9*, 359-369.
71. Colpas, G. J.; Maroney, M. J.; Bagyinka, C.; Kumar, M.; Willis, W. S.; Suib, S. L.; Mascharak, P. K.; Baidya, N., X-ray spectroscopic studies of nickel complexes, with application to the structure of nickel sites in hydrogenases. *Inorg. Chem.* **1991,** *30*, 920-928.
72. Zhang, X.; Huang, D.; Chen, Y.-S.; Holm, R. H., Synthesis of Binucleating Macrocycles and Their Nickel(II) Hydroxo- and Cyano-Bridged Complexes with Divalent Ions: Anatomical Variation of Ligand Features. *Inorg. Chem.* **2012,** *51*, 11017-11029.
73. Bahnmüller, S.; Plotzitzka, J.; Baabe, D.; Cordes, B.; Menzel, D.; Schartz, K.; Schweyen, P.; Wicht, R.; Bröring, M., Hexaethyltripyrrindione (H3Et6tpd): A Non-Innocent Ligand Forming Stable Radical Complexes with Divalent Transition-Metal Ions. *Eur. J. Inorg. Chem.* **2016,** *2016*, 4761-4768.
74. Bryngelson, P. A.; Arobo, S. E.; Pinkham, J. L.; Cabelli, D. E.; Maroney, M. J., Expression, reconstitution, and mutation of recombinant Streptomyces coelicolor NiSOD. *J. Am. Chem. Soc.* **2004,** *126*, 460-461.

75. Tietze, D.; Koley Seth, B.; Brauser, M.; Tietze, A. A.; Buntkowsky, G., NiII Complex Formation and Protonation States at the Active Site of a Nickel Superoxide Dismutase-Derived Metallopeptide: Implications for the Mechanism of Superoxide Degradation. *Chem. Eur. J.* **2018,** *24*, 15879-15888.
76. Riddles, P. W.; Blakeley, R. L.; Zerner, B., [8] Reassessment of Ellman's reagent. In *Methods Enzymol.*, Academic Press: 1983; Vol. 91, pp 49-60.
77. Ravel, B.; Newville, M., ATHENA, ARTEMIS, HEPHAESTUS: data analysis for X-ray absorption spectroscopy using IFEFFIT. *J. Synchr. Rad.* **2005,** *12*, 537-541.
78. Boiocchi, M.; Fabbrizzi, L.; Foti, F.; Vázquez, M., Further insights on the high–low spin interconversion in nickel(ii) tetramine complexes. Solvent and temperature effects. *Dalton Trans.* **2004**, 2616-2620.
79. Beauchamp, C.; Fridovich, I., Superoxide dismutase: Improved assays and an assay applicable to acrylamide gels. *Anal. Biochem.* **1971,** *44*, 276-287.
80. Tabbi, G.; Driessen, W. L.; Reedijk, J.; Bonomo, R. P.; Veldman, N.; Spek, A. L., High Superoxide Dismutase Activity of a Novel, Intramolecularly Imidazolato-Bridged Asymmetric Dicopper(II) Species. Design, Synthesis, Structure, and Magnetism of Copper(II) Complexes with a Mixed Pyrazoleâˆ'Imidazole Donor Set. *Inorg. Chem.* **1997,** *36*, 1168-1175.
81. Neese, F., The ORCA program system. *Wiley Interdiscip. Rev. Comput. Mol. Sci.* **2012,** *2*, 73-78.
82. Grimme, S.; Antony, J.; Ehrlich, S.; Krieg, H., A consistent and accurate ab initio parametrization of density functional dispersion correction (DFT-D) for the 94 elements H-Pu. *J. Chem. Phys.* **2010,** *132*, 154104-154104.
83. Grimme, S.; Ehrlich, S.; Goerigk, L., Effect of the damping function in dispersion corrected density functional theory. *J. Comput. Chem.* **2011,** *32*, 1456-1465.
84. Schäfer, A.; Horn, H.; Ahlrichs, R., Fully optimized contracted Gaussian basis sets for atoms Li to Kr. *J. Chem. Phys.* **1992,** *97*, 2571-2577.
85. Weigend, F.; Ahlrichs, R., Balanced basis sets of split valence, triple zeta valence and quadruple zeta valence quality for H to Rn: Design and assessment of accuracy. *Phys. Chem. Chem. Phys.* **2005,** *7*, 3297-3305.
86. Neese, F., An improvement of the resolution of the identity approximation for the formation of the Coulomb matrix. *J. Comput. Chem.* **2003,** *24*, 1740-1747.
87. Neese, F.; Wennmohs, F.; Hansen, A.; Becker, U., Efficient, approximate and parallel Hartree–Fock and hybrid DFT calculations. A 'chain-of-spheres' algorithm for the Hartree–Fock exchange. *Chem. Phys.* **2009,** *356*, 98-109.
88. Yanai, T.; Tew, D. P.; Handy, N. C., A new hybrid exchange–correlation functional using the Coulomb-attenuating method (CAM-B3LYP). *Chem. Phys. Lett.* **2004,** *393*, 51-57.
89. Sinnecker, S.; Rajendran, A.; Klamt, A.; Diedenhofen, M.; Neese, F., Calculation of Solvent Shifts on Electronic g-Tensors with the Conductor-Like Screening Model (COSMO) and Its Self-Consistent Generalization to Real Solvents (Direct COSMO-RS). *J. Phys. Chem. A* **2006,** *110*, 2235-2245.

Table of contents
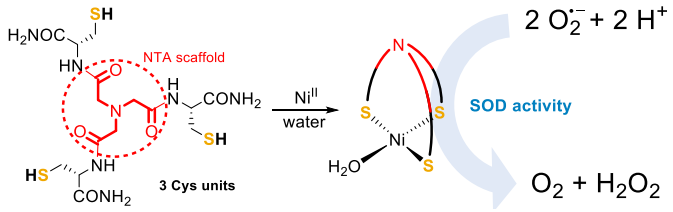
The present work reports on the synthesis and detailed characterization of bio-inspired mononuclear Ni(II) complexes based on a sulfur-rich pseudo-peptide ligand, including the first low-weight synthetic Ni(II) complex that displays catalytic SOD activity, in water, at physiological pH. The overall set of data evidences that the presence of a labile ligand (water molecule) in the coordination sphere of the Ni(II) ion is required for optimal activity, in agreement with an inner sphere mechanism.